Available online at www.sciencedirect.com
ScienceDirect
Physics of the Earth and Planetary Interiors 157 (2006) 257–268
PHYSICS OF THE EARTH AND PLANETARY INTERIORS
www.elsevier.com/locate/pepi

Small scale shallow attenuation structure at Mt. Vesuvius, Italy

Edoardo Del Pezzo[a,*], Francesca Bianco[a], Luca De Siena[a], Aldo Zollo[b]

[a] *Istituto Nazionale di Geofisica e Vulcanologia, Osservatorio Vesuviano, Napoli, Italy*
[b] *Dipartimento di Scienze Fisiche, Università di Napoli Federico II, Italy*

Received 27 January 2006; received in revised form 18 April 2006; accepted 20 April 2006

Abstract

We present a high resolution 3D model of S-wave attenuation (Q_S^{-1}) for the volcanic structure of Mt. Vesuvius. Data from 959 waveforms relative to 332 volcano-tectonic earthquakes located close to the crater axis in a depth range between 1 and 4 km (below the sea level) recorded at 6 three-component seismic stations were used for the inversion. We obtained the estimate of Q_S^{-1} for each source–station pair using a single-station method based on the normalization of the S-wave spectrum for the coda spectrum at 12 s lapse time. This is a modification of the well known coda-normalization method to estimate the average Q_S^{-1} for a given area. We adopt a parabolic ray-tracing in the high resolution 3D velocity model which was previously estimated using almost the same data set; then we solve a linear inversion scheme using the L-squared norm with positive constraints in 900 m-side cubic blocks, obtaining the estimate of Q_S^{-1} for each block. Robusteness and stability of the results are tested changing in turn the input data set and the inversion technique. Resolution is tested with both checkerboard and spike tests. Results show that attenuation structure resembles the velocity structure, well reproducing the interface between the carbonates and the overlying volcanick rocks which form the volcano. Analysis is well resolved till to a depth of 4–5 km. Higher Q contrast is found for the block overlying the carbonate basement and close to the crater axis, almost cohincident with a positive P-wave velocity contrast located in the same volume and previously interpreted as the residual high density body related to the last eruptions of Mt. Vesuvius. We interpret this high-Q zone as the upper part of carbonate basement in which most of the high energy seismicity take place. The low-Q values found at shallow depth are interpreted as due to the high heterogeneity mainly caused by the mixing of lava layers and pyroclastic materials extruded during the last eruptions.

Keywords: Attenuation tomography; Mt. Vesuvius; Coda normalization method

1. Introduction

Mt. Vesuvius, dormant since the last eruption in 1944, is considered as the most potentially dangerous volcano in the world, due to the presence of more than 700.000 people living in an area radially extended less than 15 km from the crater. Crucial for the people evacuation in case of eruption renewal is the correct establishment of possible scenarios, each one based on a volcanological model. Extreme scenarios are those related to the occurrence of a plinian (that destroyed Pompei in 79 d.C.), or a sub-plinian eruption, like those of 472 or 1631 A.D (Scandone et al., 1993); The debate about the choice of the reference scenario for the revision of the actual evacuation plans from the Civil Protection of Italy is quite animated. The development of any scenario needs a structural model of the volcano, and in particular the details about the location

* Corresponding author. Tel.: +39 081 6108324; fax: +39 081 6108 323.
E-mail address: delpezzo@ov.ingv.it (E. Del Pezzo)..

0031-9201/$ – see front matter ©2006 Elsevier B.V. All rights reserved.
doi:10.1016/j.pepi.2006.04.009

and the volume of the possible magma patches underneath.

Geophysics, and in particular seismology, provide useful tools for partially answering to this question. TOMOVES results (see the book by Capuano et al. (2003) and the numerous references therein) have provided the clearest picture actually available of the geological structure underneath Mt. Vesuvius. The most important result from TOMOVES is the existence of a magma sill at 8–10 km depth, inferred by the presence of a P to S conversion at a reflecting interface representing the top of this sill. Lateral extension is not well defined even though it is thought wide enough to reach the border of Campi Flegrei volcano, located about 20 km Eastward.

First-P arrival times from The TOMOVES project also provided refined 2D and 3D P-velocity models for the upper 4–5 km underneath the whole Campanian Plain Zollo et al. (2002) and Lomax et al. (2001). The inferred 2D images of Mt. Vesuvius and Campanian Plain show a sharp P-velocity increase at a depth range of 2000–3000 m. This is attributed to a vertical transition between the Plio-quaternary volcano-sedimentary sequence and Mesozoic limestone basement. The limestone top appears to have an irregular shape and generally dips from the edges of the Campanian Plain toward the Mt. Vesuvius volcano, consistently with the Bouguer anomalies pattern Cassano and La Torre (1987) and Berrino et al. (1993).

Recently, the last 5 km underneath the ground level have been investigated by tomographic inversion of first-P arrival times from microearthquakes (Scarpa et al., 2002) reaching a resolution of about 300–500 m. Results from this study allowed for a precise relocation of the local seismicity, almost all of volcano-tectonic type, in two space clusters separated by a zone of positive V_p contrast; the main results are: (a) the presence of a high V_p velocity body beneath the crater, surrounded laterally by lower P-velocity volcanic rocks; and (b) the carbonate basement at 2–2.5 km beneath the sea-level (consistent with TOMOVES active seismic data modeling), at the top of which almost all the high energy and stress-drop seismicity (Del Pezzo et al., 2004) is located in axis with the crater. At the border of carbonate basement with the overlying volcanic structures the maximum magnitude earthquake ever recorded at Mt. Vesuvius in the last 40 years took place (October 9, 1999, $M = 3.6$). Zollo et al. (2002) and Scarpa et al. (2002), hereafter cited as SCA02, interpreted the tomographic structures inferred from active and passive seismic data in terms of the absence of any small magma chamber in the investigated depth range. A high V_p/V_s ratio in the upper layers (1 km below the topography) was related by SCA02 to the presence of a highly fractured aquifer, permeated by intense circulation of hot fluids.

In the present paper we add a new image of the volcanic shallow structure of Mt. Vesuvius, based on a total-Q tomographic model. We adopt a new technique to obtain the observables, based on the well known concept of coda-normalization (Aki, 1980) applied to the single station estimate of total inverse-Q along the seismic path. We trace rays in the 3D velocity model of SCA02 and invert for total inverse-Q in cubic blocks with dimension of 900 m. The technique produce stable and robust results, which indicate a structure similar to (even though with less resolution of) that inferred by SCA02. We interpret the new image jointly with the velocity tomography, giving new insight on the shallow structure of Mt. Vesuvius.

2. Data and ray tracing

We use the waveforms recorded at five digital, high dynamic (120 dB, gain ranging), 1 Hz , three component seismic stations with the addition of data from the analogical station OVO (66 dB dynamic range, three component), in operation since 1972 at the historical building of Vesuvius Observatory. Digital stations are sampled at 125 s.p.s. whereas at OVO the sampling rate is set at 100 s.p.s. Analog anti-aliasing filter with 25 Hz cut-off frequency operated on all the data logger prior to sampling. We selected for the present analysis 332 earthquakes on the base of the best signal to noise ratio, absence in the waveforms of spikes and other disturbances, and coda lasting at least till to 15 s lapse time from earthquake origin time. In doing this selection we implicitly restricted the magnitude in the range from 1.8 to 3.0, as in the coda of the earthquakes with $M > 3.0$ small aftershocks are often present. The time period investigated is January–September 1999 and January–June 2000. The total number of waveforms resulted to be 959. In Table 1 station name and coordinates are reported.

Location of the 332 earthquakes (Fig. 1) was obtained with a non linear procedure which uses a grid-search algorithm (Lomax et al., 2001) using a 3D velocity model based on results by (SCA02) . Ray length range from 0.5 to 7 km, corresponding to S-travel times from 0.3 to 3.9 s. We used an approximate ray-tracing technique to compute wave trajectories in the same velocity model utilized in the location procedure. We numerically search for the best-adapted parabolas in the vertical plane connecting source and station, satisfying the Fermat's principle of minimum travel time (Fig. 2). In this way we obtained an analytical representation of

Table 1

Station	Latitude (°)	Longitude (°)	Altitude (a.s.l.) (km)	x (km)	y (km)
BKEM	40.4909	14.2633	0.863	5.41363	3.87329
FTCM	40.4778	14.2636	0.35	5.42890	1.44879
BAFM	40.4872	14.2471	0.594	3.10806	3.18792
SGVM	40.4906	14.2485	0.734	3.30463	3.81697
BKNM	40.4977	14.2578	0.865	4.61176	5.13175
OVO	40.4965	14.2380	0.584	1.92606	4.81669

the ray-paths (three coefficients for each ray) that served to save computer time in the inversion process. The parabola coefficients for each source–receiver pair have been stored in a data base, successively used for calculations.

3. Estimate of the path attenuation and inversion scheme

The seismic total attenuation coefficient, proportional to Q_T^{-1}, the inverse total Q, is a parameter controlling the seismic energy density spectrum decay as a function of lapse time as

$$E_{ij}(f,r) = S_i(f)\theta_{ij}(\vartheta,\phi)I_j(f)T_j(f)G_{ij}(r) \times \exp\left(-2\pi f \frac{t_{ij}(r)}{Q_{\mathrm{T}}^{ij}(r)}\right) \quad (1)$$

where $E(f,r)$ is the energy density spectrum and f is the frequency of the S-wave radiation emitted by the source i at total distance r measured along the source (i)–station (j) ray-path. $S_i(f)$ is the energy spectrum at source, modulated by the radiation pattern $\theta(\vartheta,\phi)$. I_j is the instrument transfer function, T_j is the site

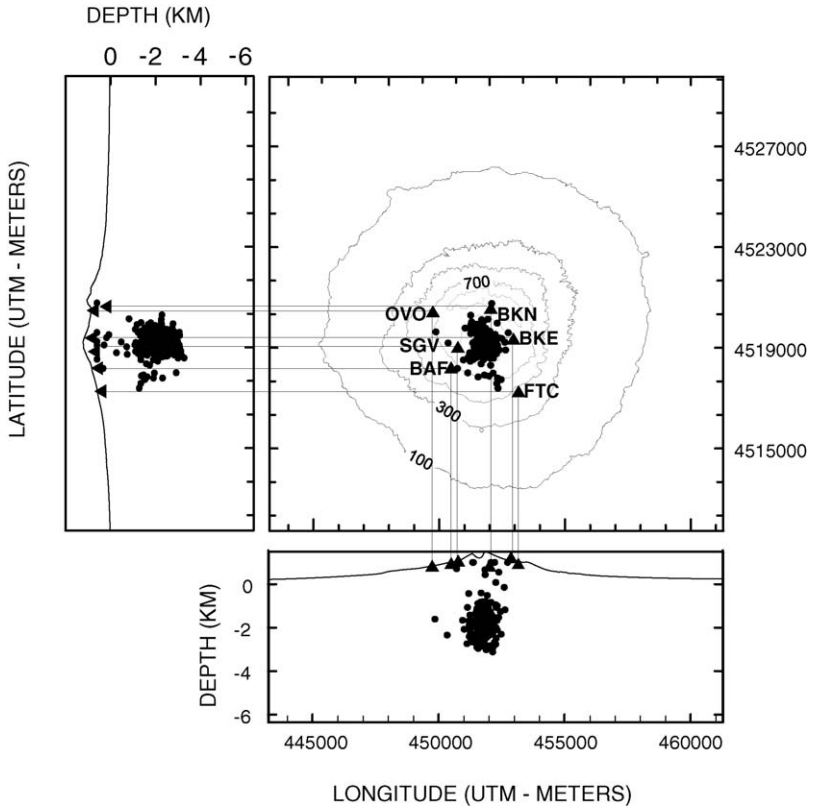

Fig. 1. Map of Mt. Vesuvius with station positions (black triangles) and hypocentral locations (black circles). Upper-left and downward panels represent the S-N and W-E sections, respectively. Continuous lines connect the station positions on the map to the correspondent location onto the sections.

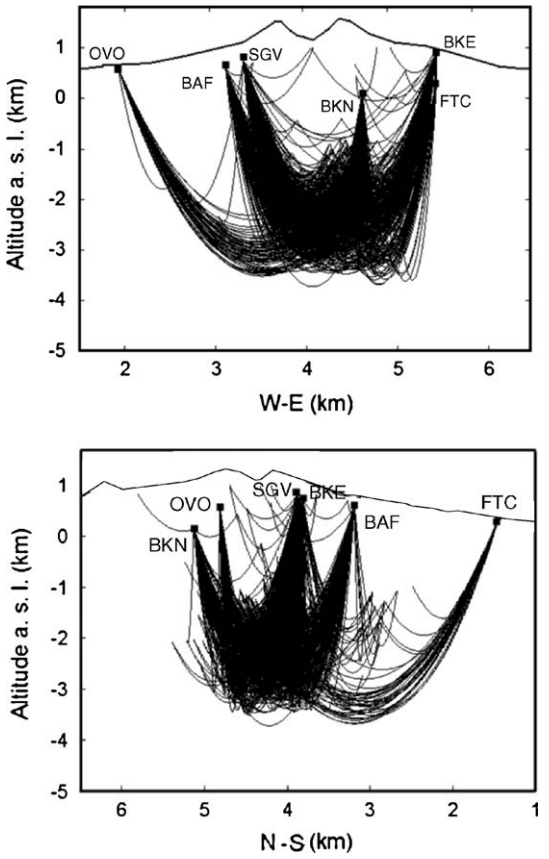

Fig. 2. Ray-path projections on E-W and N-S sections of Mt. Vesuvio for the seismic events used in the present study. Rays obtained with a parabolic ray-tracing represent the Fermat's paths of minimum travel time.

transfer function and G is the geometrical spreading term. t_{ij} is the travel time along the ray whose coordinate is r and Q_{T}^{ij} is the total quality factor measured along the ray-path. Q_{T} defines the fractional energy lost per cycle, ΔE, through the formula $Q = -2\pi E/\Delta E$.

The estimate of Q_{T}^{-1} from estimates of $E(f, r)$ is function of several factors depending on the responses of instrument, site and source. Among these terms the one that is better known is the instrument response, while site and source effects are less known. This is mostly due to the complex task of discriminating on seismograms the site and source effects. By eliminating the source and site terms in the estimate of total Q with a single station method is consequently an important pre-requisite for any attenuation tomography problem.

Based on the phenomenological properties of the coda waves, Aki (1980) expressed the coda energy spectrum, evaluated around a given lapse time, t_{c}, as a function of the "average" medium properties as

$$E^C(f, t_{\mathrm{c}}) = S_i(f) I_j(f) T_j(f) P(f, t_{\mathrm{c}}) \tag{2}$$

where $P(f, t_{\mathrm{c}})$ is independent on both source–receiver distance and directional azimuth and the radiation pattern term ($\theta_{ij}(\vartheta, \phi)$) disappears due to the well known properties of coda waves (Aki, 1980). The coda Power $P(f, t_{\mathrm{c}})$ can in principle take any analytical form as it is independent of the assumed scattering model. It depends on the average properties of the earth medium (Sato and Fehler, 1998). Here we assume the validity of the single scattering model for sake of simplicity, and hence

$$P(f, t_{\mathrm{c}}) = \frac{2 g_0}{t_{\mathrm{c}}^2 V_0^2} \exp[-2\pi f t_{\mathrm{c}} / Q_{\mathrm{c}}(f)] \tag{3}$$

where Q_{c} is the so called coda-Q, depending on frequency, g_0 is the scattering coefficient (averaged on the volume encompassed by the coda waves Sato and Fehler (1998)) and V_0 is the average velocity. Dividing Eq. 1 for Eq. 2 we obtain for each source–station pair, at lapse time t_{c}

$$\frac{E_{ij}(f, r)}{E^C(f, t_{\mathrm{c}})} = \frac{\theta_{ij}(\vartheta, \phi)}{P(f, t_{\mathrm{c}})} G_{ij}(r) \exp\left[-2\pi f \int_{\mathrm{ray}} \frac{\mathrm{d}l}{v(l) Q(l)}\right] \tag{4}$$

obtaining an expression independent of energy level at source, site and instrument transfer function. In formula (4) the attenuation operator has been substituted with the path integral along the seismic ray, where $v(l)$ is the velocity along the path l. $\theta_{ij}(\vartheta, \phi)$ in principle depends on source azimuth ϕ and incidence angle ϑ.

We make the assumption that this dependence becomes negligible when the estimate of $E_{ij}(f, r)$ of Eq. (4) is made on a time window of duration much greater than the source duration (Gusev and Abubakirov, 1999). This assumption is based on the following simple conceptual model. Source pulse signals propagates along the ray path. Their amplitude and duration depends on the seismic moment rate function. In case of small ($M < 3$) earthquakes, the source pulse duration is of the order of 0.2 s, given an expected source size of few hundreds of meters. The seismic pulses following the direct wave are generated by the interaction of the primary pulse with the earth medium heterogeneities. These can be assumed randomly located inside a volume surrounding the seismic ray. This sort of ray tube is the volume where the scattering processes generate the wave packet in the first few seconds of seismogram after the direct S-arrival. Due to the random nature of the scattering process, the seismic radiation in the time window of duration T starting at the S-wave first arrival is a sort of natural average

produced in a wide range of directions from the station and hence becomes independent on ϑ and ϕ at increasing T. We made a test confirming the validity of this assumption that will be described later in the present paper.

Taking $G(r)=r_0^2/r^2$, where r is the total length of the seismic ray and r_0 a reference length set at 1 km, and transforming energy in amplitude, Eq. (4) may be written as

$$\ln\left(\frac{|A_{ij}^{S}(f)|}{|A_{ij}^{C}(f,t_c)|}\cdot r_{ij}\right) = K(f,t_c) - \pi f \int_{r_{ij}} \frac{dl}{v(l)Q(l)}, \tag{5}$$

where A_{ij}^{S} and A_{ij}^{C} are the spectral amplitudes of respectively S and coda, $K(f,t_c)$ is constant for each frequency band, depending only on the average properties of the earth medium and r_{ij} is the total length of the seismic ray for the couple ij. Introducing the slowness $s(l)=1/v(l)$, and discretizing we can write

$$R_{ij} = K(f) - \pi f \sum_{b=1}^{B} l_{ijb} s_b Q_b^{-1}, \tag{6}$$

where R_{ij} represents the log of amplitude spectral ratio premultiplied by r; index b indicates the b-th block in which the earth medium is divided and B is the number of blocks. s_b and l_{ijb} are, respectively the slowness and the length of the ray-segment crossing the bth block. Eq. (6) can be linearly inverted for Q_b^{-1}.

4. Data analysis and results

4.1. Test of independence from radiation pattern

We first visually check how much the quantity R_{ij} varies with S-wave window duration T. We observe that for $T > 3$ s, R_{ij} does not significantly vary with the window length. This should imply that a certain stability for the estimate of R_{ij} is reached for 3 s window duration. Then we select few events among those with high signal to noise ratio at all the stations. After correcting the amplitudes for geometrical spreading and for the average Q already estimated for the same area by Bianco et al. (1999) we estimate the log of spectral ratio between direct S radiation and coda radiation for each station (we average over the two horizontal components of the ground motion). Coda window starts at lapse time of 8 s and ends at 12 s. Then we average over the stations and estimate the standard deviation σ. This procedure is repeated for different values of time duration of the S-wave window. As an example, we plot

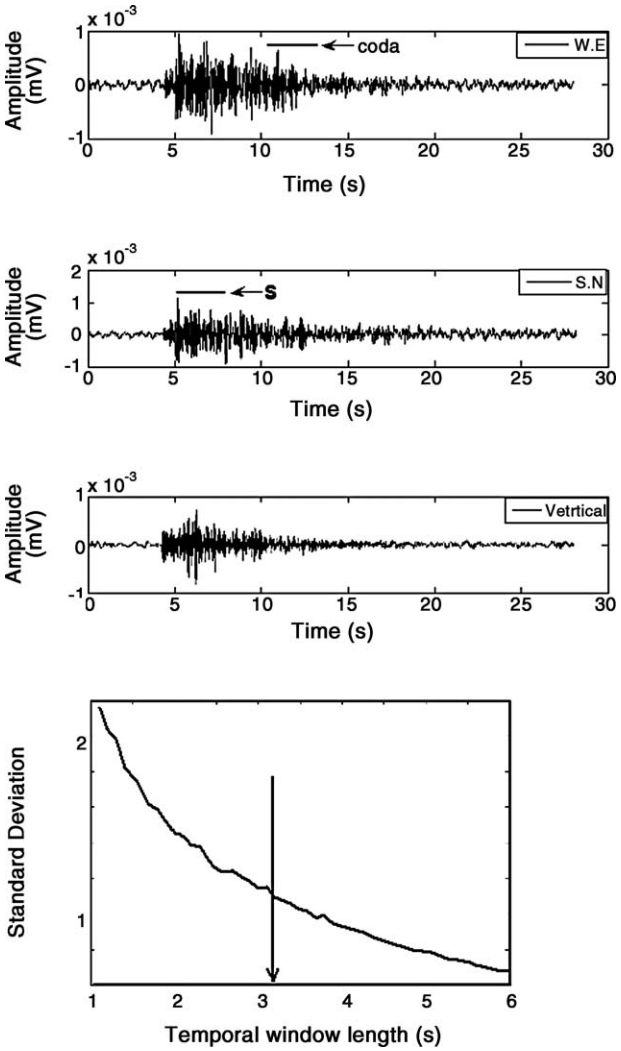

Fig. 3. The standard deviation, σ, obtained calculating the average (over stations) of the log of spectral ratio between direct S radiation and coda radiation, after correcting the amplitudes for geometrical spreading and for the average Q, is represented in the lower panel as a function of the time window duration, for a quake recorded at all the stations (an example at BKE station is reported in the upper panel). Downward arrow indicate the empirically determined optimal window length.

in Fig. 3 σ as a function of the time window duration for a quake recorded at all stations. From the pattern of σ we deduce that after around 3 s of duration, the standard deviation of the spectral ratio averaged over the stations falls below 70% of the maximum. Interpreting the fluctuations around the average as mainly produced by radiation pattern effects, we deduce from this pattern as an indirect confirmation of validity for the assumption made in the conceptual model described above.

Table 2

f_{low}	$f_c(Hz)$	f_{high}
2.4	3	3.6
4.7	6	7.2
8.2	12	15.8
12.4	18	23.6

4.2. Estimate of the observables, discretization, and inversion technique

For the considerations above reported, we set the duration of the S-waves time window at 3 s starting from the S-wave travel time. Coda signal time window starts at 8s lapse time and ends at 12 s. We set this value (12 s) because for most of data utilized the signal-to-noise ratio is greater than three for lapse times smaller than 12 s. An FFT is applied to the windowed signals (we used a cosine taper window with tapering at 10% both for S and coda) for both the horizontal components of the ground motion. The spectral amplitude is log-averaged over the components in the frequency bands centered at f_c with bandwidths ($\pm\Delta f$), as reported in Table 2 is then calculated, and finally the ratio between the S-wave window and the coda window is calculated.

The natural logarithm of the ratio is premultiplied by the ray path length to obtain an estimate of R_{ij}. R_{ij} is calculated for the two horizontal components. The earth volume under study has the surface extension of 9 km × 9 km and a depth extension of 4.5 km. We discretized this volume by a cubic grid with spacing of the grid nodes chosen on the base of two main criteria: the first is that the wavelength must be smaller than the grid spacing (the wavelength of the seismic signals utilized in this work span from 0.1 to 0.6 km); the second is that the ray density in each grid volume-cell must be sufficiently high to guarantee a robustness of the inversion and an optimal resolution. We calculate the intersections of the ray paths with volume cells, obtaining the quantities l_{ijb}. s_b, the slowness in each volume cell, is the average in the volume cell of the slowness values taken from velocity tomography (SCA02). The constant K (see formula (6)) in the assumption of single scattering is given by

$$K = \frac{t_c^2 V_0^2}{2g_0} \exp\left(\frac{2\pi f t_c}{Q_c}\right) \tag{7}$$

and can be independently estimated from the already determined estimates of Q_c (Bianco et al., 1999) and g_0 (Del Pezzo et al. submitted for publication) that are reported in Table 3.

We can invert the problem expressed by formula (6) simultaneously for K and the set of Q^{-1} , or we can a-priori set K to the value already estimated and resolve only for the set of Q^{-1}.

The inversion problem can be rewritten for sake of compactness in a simpler way, changing the couple of indexes ij in a single integer index, k. k ranges from 1 to N_pairs where N_pairs is the number of source station pairs, and designates the corresponding ray-path. Analogously, N_cells indicates the total number of blocks. Denoting $K(f)/\pi f$ as $C(f)$ we rewrite formula (6) as

$$C(f) - \frac{R_k}{\pi f} = \sum_{b=1}^{N\_cells} l_{kb} s_b Q_b^{-1} \tag{8}$$

In vectorial form, representing the suite of the ray-paths,

$$\mathbf{d}(f) = \mathbf{G}\mathbf{m}(f) \tag{9}$$

where $\mathbf{d}$ contain the calculated spectral ratios for each frequency band, averaged over the two horizontal components of ground motion, for all the ray-paths. $\mathbf{G}$ is a

Table 3

Station	$f_c = 3$ Hz	$f_c = 6$ Hz	$f_c = 12$ Hz	$f_c = 18$ Hz
Q-coda inverse				
BKEM	7.7	4.9	5.2	3.9
FTCM	8.1	5.3	3.7	4.2
SGVM	6.4	7.1	5.6	4.7
BKNM	8.0	4.7	5.9	4.7
OVO	7	6.8	6.5	6.4
f_c				$\langle g_0 \rangle$
3 Hz				1.9
6 Hz				2.1
12 Hz				1.6
18 Hz				1.5

Q-coda inverse ($\cdot 10^3$) estimated by Bianco et al. (1999) and $\langle g \rangle$, the average scattering coefficient, estimated by Del Pezzo et al. (submitted for publication).

rectangular sparse matrix as

$$\mathbf{G} = \begin{bmatrix} l_{11}s_1 & l_{12}s_2 & \cdot & l_{1b}s_b & 0 & \cdot & l_{1N\_\text{cells}}s_{N\_\text{cells}} \\ l_{21}s_1 & l_{22}s_2 & \cdot & 0 & 0 & \cdot & l_{2N\_\text{cells}}s_{N\_\text{cells}} \\ \cdot & \cdot & \cdot & \cdot & \cdot & \cdot & \cdot \\ \cdot & 0 & \cdot & l_{kb}s_b & \cdot & 0 & \cdot \\ \cdot & \cdot & \cdot & \cdot & \cdot & \cdot & 0 \\ 0 & \cdot & \cdot & \cdot & \cdot & \cdot & \cdot \\ \cdot & \cdot & \cdot & \cdot & \cdot & \cdot & \cdot \\ l_{N\_\text{pairs}1}s_1 & \cdot & \cdot & 0 & \cdot & \cdot & l_{N\_\text{pairs}N\_\text{cells}}s_{N\_\text{cells}} \end{bmatrix}$$

and **m** is the column vector containing the estimates of Q^{-1} for each volume cell. The problem can be solved separately for each frequency band. The inversion is linear and needs to be constrained to obtain only positive values of Q^{-1}. We solve the problem using the positive least squares algorithm "lsqnonneg" deployed in MATLAB (Lawson and Hanson, 1974).

4.3. Resolution

We determined the optimal dimension of the cubic cell together with the resolution of the method with a trial and error approach. We base our test on two synthetic images, the first consisting of a high Q-contrast block, 0.9 km × 1.8 km located in central position respect to the crater (see Fig. 4a) and the second of a checkerboard structure, with high Q-contrast among the blocks (Fig. 4b). We use the ray-tracing with the same configuration of sources and stations as that associated with the real data, and calculate the synthetic S-to-coda spectral ratios, adding log-normally distributed noise with a percent standard deviation of 15%. Then we invert using the inversion scheme (9) and by trial and error determine the minimum cell dimension (fulfilling the restriction that must be greater than the maximum wavelength, as already discussed above). We selected the minimum cell dimension as that reasonably well reproduces the in-

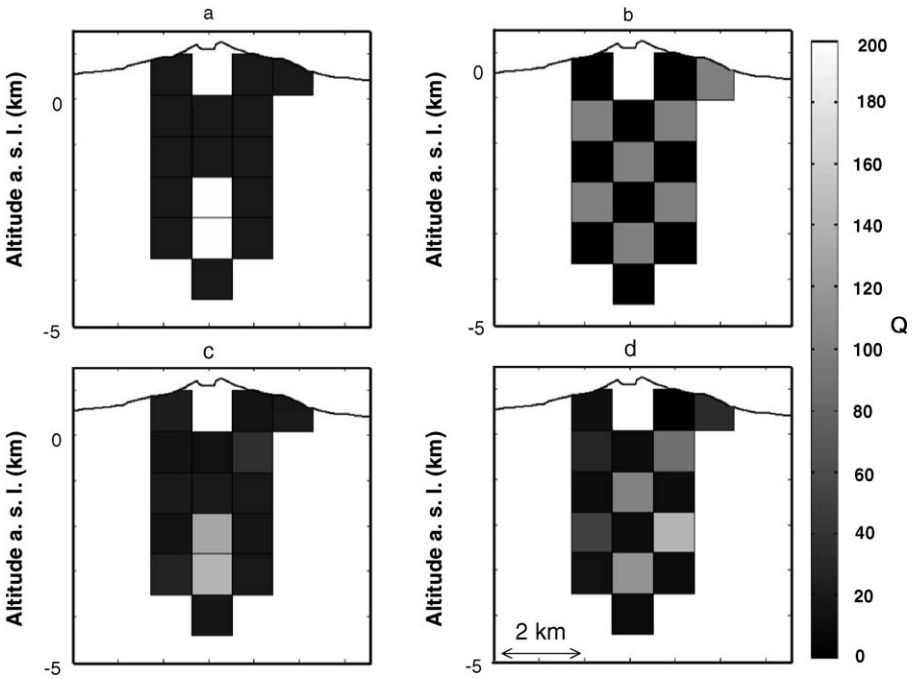

Fig. 4. Resolution tests based on two synthetic images. Panel a represents a high Q-contrast block, 0.9 km × 1.8 km located in central position respect to the crater; panel b represents a checkerboard structure, with high Q-contrast among the blocks . Test results (respectively panel c and d) reproduce the input values within less than 30% of uncertainty for cells crossed by a minimum of 40 rays. Grey scale represents the Q-value scale utilized.

Table 4

Block#		1	2	3	4	5	6	7	8
Robusteness test									
Q		33	29	185	72	122	139	262	440
σ (from Covariance)		1	1	3	8	20	14	20	110
σ, 5% of data reduction		1	1	5	16	17	34	35	119
σ, 10% of data reduction		1	1	7	19	27	42	43	169
σ, 20% of data reduction		4	7	7	23	57	64	76	220
σ, 30% of data reduction		304	97	157	29	349	202	115	283
Block#	1	2	3	4	5	6	7	8	
Stability test									
Q	33	29	185	72	122	139	262	440	
Q, g_{min}	33	29	185	72	122	139	262	439	
Q, g_{max}	33	29	185	72	121	138	263	440	

Robusteness and stability. The upper table reports for eight blocks the estimate of Q from the inversion process applied to the entire data set (first row), the variance of this estimate (second row) and the variances calculated from the tests applied to a reducted number of equations. Till to a 20% of reduction results show robusteness in the solution. The lower table reports for the same eight blocks the values of Q from the inversion process (upper row) and those obtained fixing the g_0 value of formula (7) at the extremes of the confidence interval.

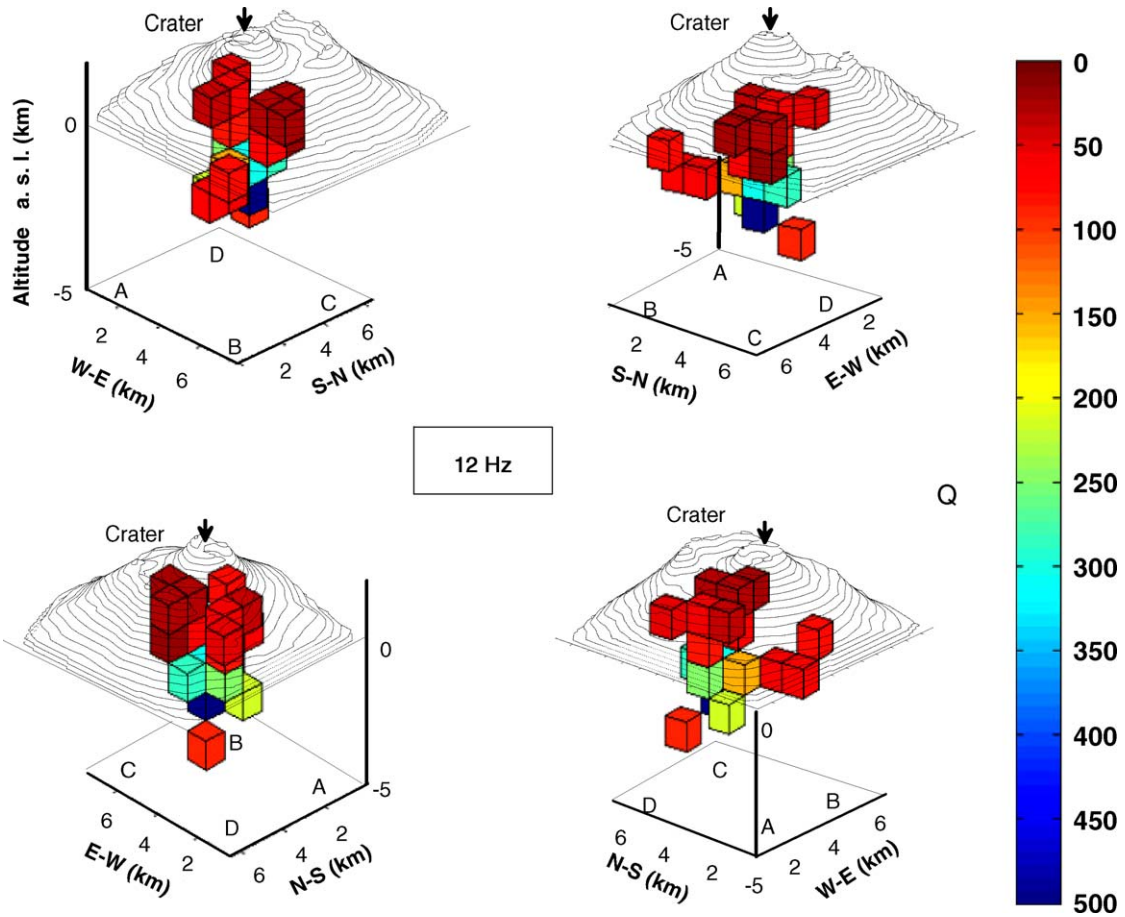

Fig. 5. Tomography results, obtained for the frequency band centered at 12 Hz. We use four different perspectives, each one shifted by 90°. The main features of the attenuation structure of Mt. Vesuvius are essentially a laterally uniform low Q region in the first 1.8 km of crust (from the top) under the volcano, and a heterogeneous Q-structure below this depth.

put image. In these test we empirically observe that cells crossed by a minimum of 40 rays reproduce the input values within less than 30% uncertainty. The cell dimension of 0.9 km results to be optimal. Fixing this volume cell dimension and representing the results for the sole cells crossed by more than 40 rays, the two synthetic images result well resolved (Fig. 4c and d).

The robustness of the method is tested using a bootstrap approach Lees and Crosson (1989) and Tichelaar and Ruff (1989) We reduced the number of equations of 5%, 10%, 20% and 30% with a random extraction, obtaining, for each percent group, 100 data set. For each of these data set we resolved the inversion process, and estimated the Q factor and its standard deviation for each block from the average of the 100 solutions. Then, we compare these solutions with the solution obtained from the whole data set (and with its covariance matrix). We observe a significative increase in standard deviation for the random extraction of 30% of data, whereas for that obtained for 5%, 10% and 20% the standard deviation is comparable with that from the entire data set. We report in Table 4 the output of this test (obtained at 18 Hz central frequency) for a number of eight selected blocks.

Stability of the solution is indirectly tested by changing the value of the constant $C(f)$ in formula (8), letting g_0 of Eq. (7) to vary between the values of $g_{\min} = 1$ and $g_{\max} = 2.5$ that represent the error limits of this estimates as reported by Del Pezzo et al. (submitted for publication). Results from these tests ensure that the solution obtained is practically insensitive to $C(f)$ as reported in Table 4 for the same suite of eight selected blocks reported for the robusteness test.

4.4. Results

We show in Figs. 5 and 6 the results obtained for the frequency bands centered at 12 and 18 hz. In the band centered at 6 hz signal to noise ratio at 12 s lapse time is often below the threshold. This implies that we consider for the inversion a limited data set. Consequently, results for the band centered at 6 hz show that at this frequency only few blocks can be resolved, and consequently are not considered here. The main features of the attenuation structure of Mt. Vesuvius are essentially a laterally uniform low Q region in the first 1.8 km from the top of the volcano, and an heterogeneous Q-structure below this depth. In the E-W sections (Fig. 7b and 8b) an high Q zone (blue and green colored blocks) centrally located respect to the crater axis, surrounded by lower-Q blocks can be easily visualized. The results obtained at 18 hz are better defined than those at 12 hz showing five additional resolved blocks. The high Q contrast blocks are

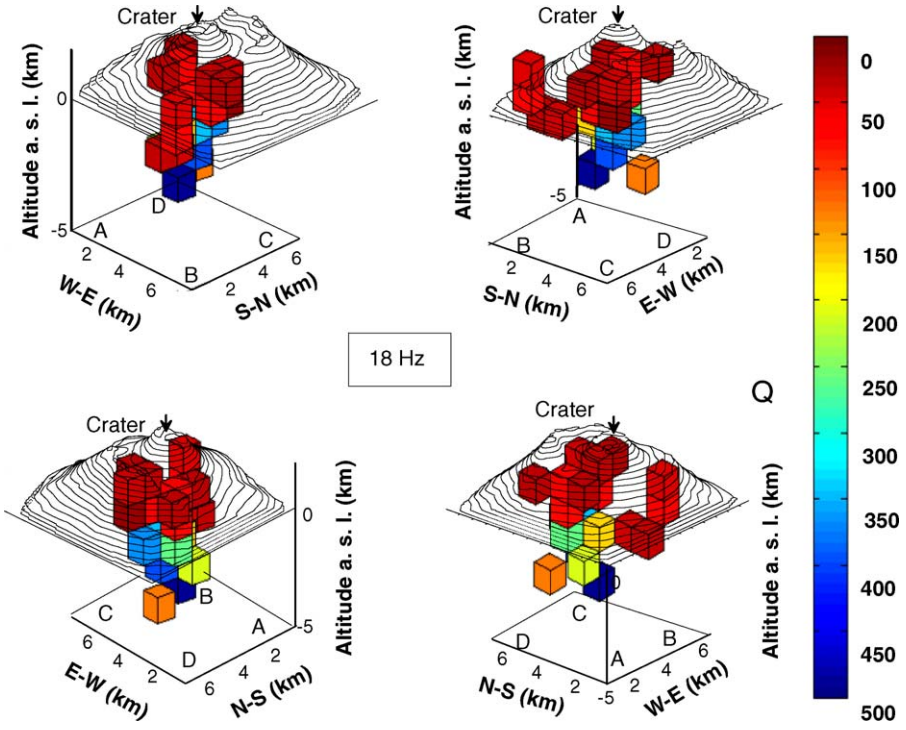

Fig. 6. The same of Fig. 5, for the frequency band centered at 18 Hz. In this frequency band, the high-Q zone located at approximately 3 km b.s.l. is more evident than that imaged at 12 Hz.

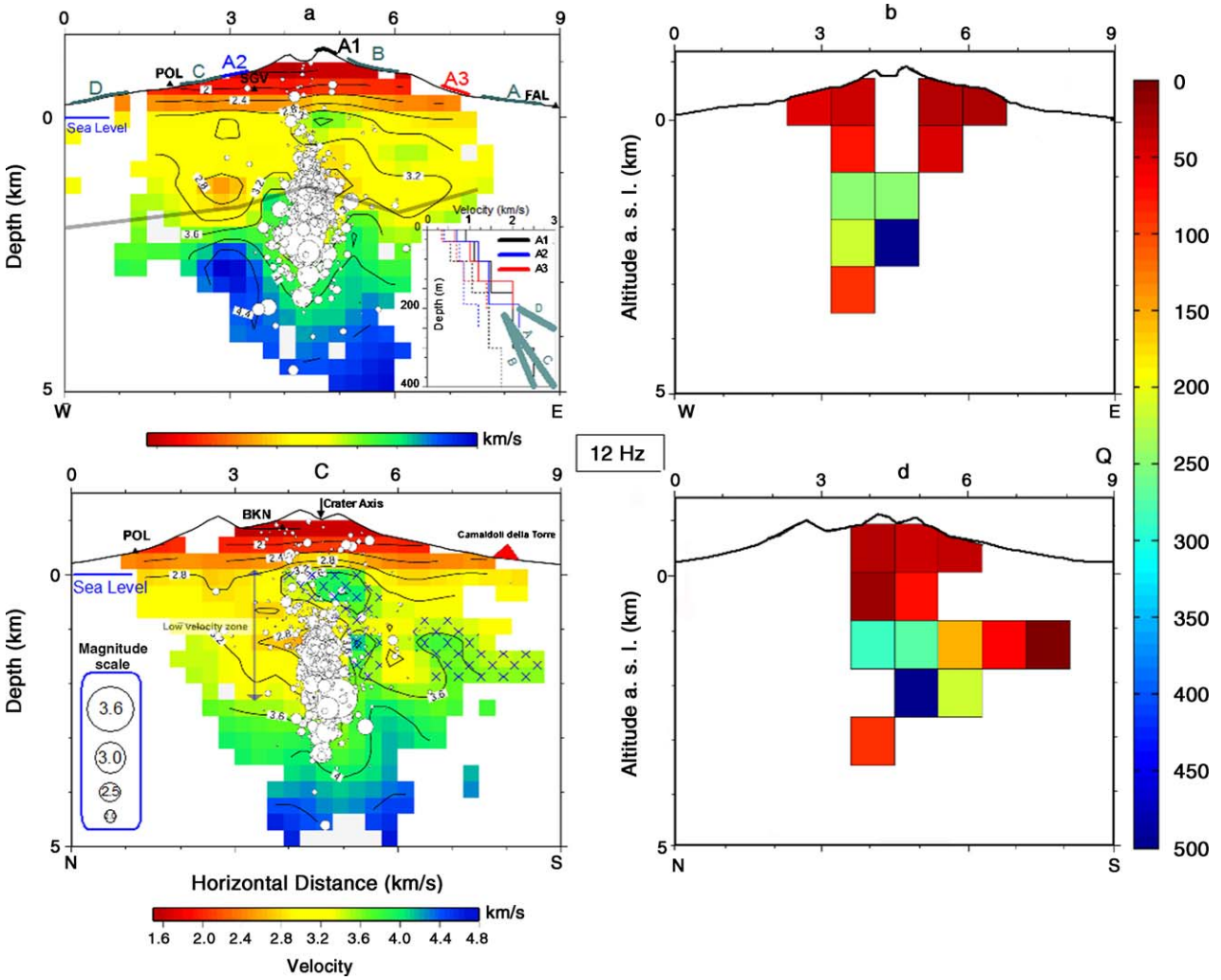

Fig. 7. Q-tomography results, obtained for the frequency band centered at 12 Hz, representing W-E (panel b) and S-N (panel d) sections of the earth structure. The high Q contrast blocks have a pattern similar to that of the high velocity zones in the (a) W-E and (c) N-S cross sections of the P-wave velocity structure inferred by the travel time tomography (SCA02). In panels a and c white circles show the relocated hypocenters having size proportional to magnitude and the low velocity layer toward N is linked to the deepening of the limestone basement.

distributed in space similarly to the high velocity zones inferred by the travel time velocity tomography (SCA02) which has been utilized in the present study for the ray tracing, reported in the same figures for sake of comparison. This high velocity zone has been interpreted by SCA02 as the upper part of the limestone basement and is consistent with the depth of the limestone top retrieved from active seismic tomography underneath Mt. Vesuvius using the TOMOVES data set Zollo et al. (2002).

5. Discussion and conclusions

In the present paper we have measured the total attenuation for S waves with a method almost independent of site and radiation pattern, obtaining a tomography image of Mt. Vesuvius. As the S-wave high attenuation zones may be indicative of the presence of magma patches, the application of the present methodology is particularly suitable to the study of volcanic areas (Figs. 7 and 8).

The total attenuation is represented by the inverse quality factor, Q_{T}^{-1} , that can be expressed as

$$Q_{\mathrm{T}}^{-1} = Q_{\mathrm{i}}^{-1} + Q_{\mathrm{Sc}}^{-1} \tag{10}$$

where Q_{i}^{-1} is the inverse of the intrinsic quality factor and Q_{Sc}^{-1} is the inverse of the scattering quality factor (Sato and Fehler, 1998). How total Q is separated into its parts needs to be known in order to correctly interpret the attenuation images. The interpretation of the present

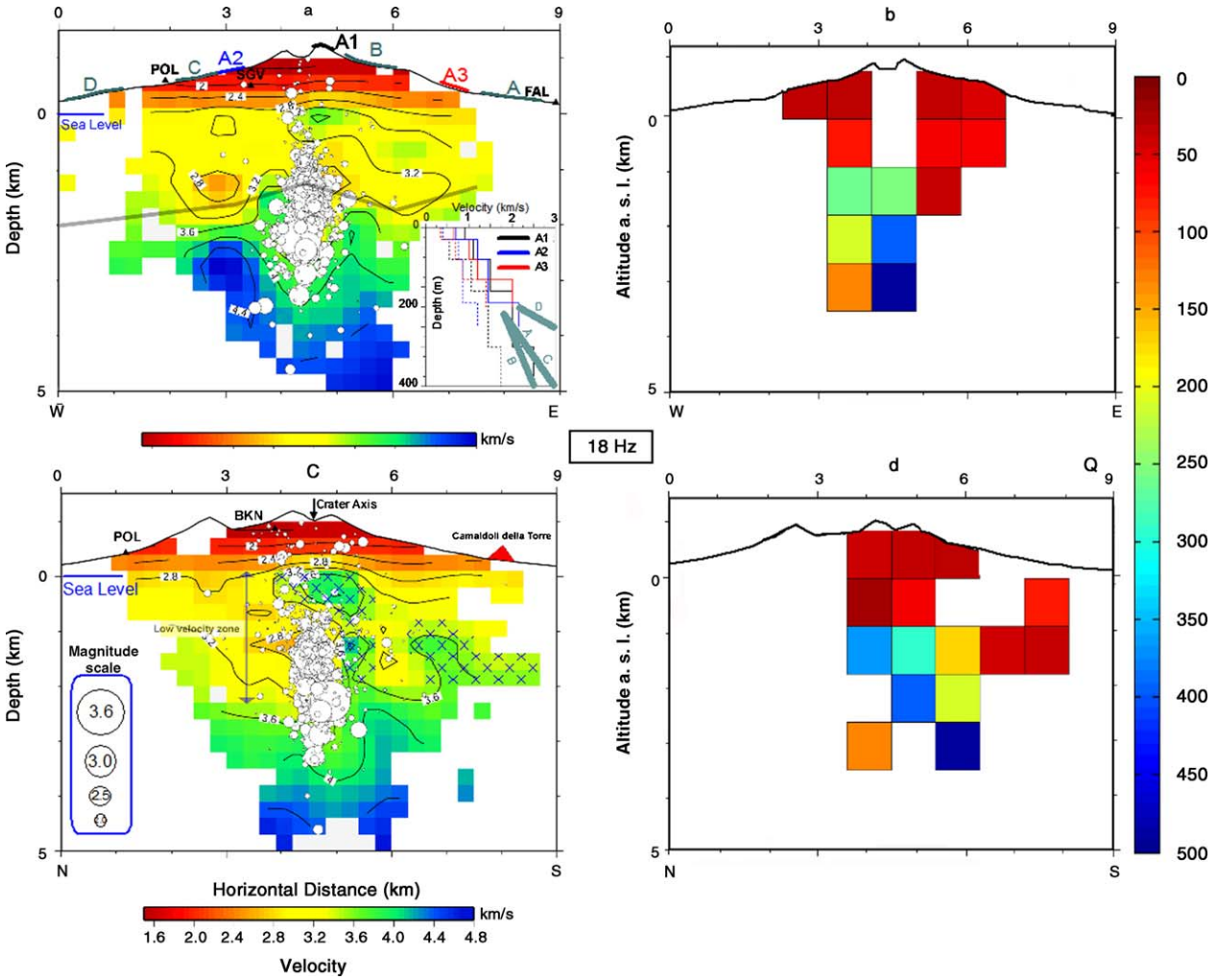

Fig. 8. The same of Fig. 7, for the frequency band of 18 Hz.

results may be facilitated by considering the results of a previous study (Bianco et al., 1999) on seismic attenuation on Mt. Vesuvius, and by a more recent observation, concerning a reappraisal of the separated Q_i^{-1} and Q_{Sc}^{-1} parameters, averaged on the entire volcano (Del Pezzo et al., submitted for publication). These two studies indicate that Q_{Sc}^{-1} could dominate in average over Q_i^{-1}. Thus, we think that the observed Q-anomalies may be attributed predominantly to variations of scattering Q. The low-Q materials composing the shallow structure of Mt. Vesuvius (quality factors as low as less than 50) should indicate high heterogeneity. We attribute this heterogeneity to the presence of a mixture of indurated lava flows and relatively inconsolidated pyroclastic materials, associated with the past eruptive activity of this volcano. This zone reaches a depth of about 2 km under the top of topography. Q-Tomography also evidences a zone with high Q, which coincides with the zones with highest P-wave velocity where most of the largest earthquakes occurs. This zone should be the less heterogeneous. We think that it may be partly composed by the upper part of limestone basement under the volcano with a high homogeneity and high rigidity respect to the surrounding rocks. We consequently exclude that this high-Q body is composed by the residual magma bodies emplaced during the last 1944 and preceding eruptions. In synthesis, the S-wave attenuation tomography reproduces the same features of the P-velocity tomography even though the resolution of the attenuation tomography is poorer (a half of that associated with velocity tomography) and can be interpreted in the same way. This similarity consequently reinforces one of the interpretation already done by SCA02, that there are no evidences of a shallow magma body in the first 4 km below the ground

surface. The absence of shallow magma chambers can be considered as an important constraint to be put on any dynamical model of Mt. Vesuvius. The inferences that can be made on the base of the present results can be summarized in the following main points:

- Largest earthquakes are located in a zone of relatively high rigidity, possibly constituting the top part of the limestone basement under Mt. Vesuvius, as described in SCA02 and in (Lomax et al., 2001). The presence of this high rigidity layer is clearly reproduced also by the attenuation imaging, that indicates a zone of relatively high total-Q.
- Shallowest materials are composed by an heterogeneous structure, composed by the mixing of lava layers and pyroclastic materials extruded during the last eruptions. A pronounced aquifer below the central crater should have been the predominant cause of many past eruptions, as many hydrothermal events have been observed during plinian and sub-plinian events. The present data are not in contrast with this evidence, as the high scattering attenuation in the shallow part of the volcanic structure is compatible with the presence of shallow aquifers.
- There is no evidence of shallow patches of low-Q materials at the depth between 2 and 3 km, at least at the resolution scale of this study. This should imply that the shallow magma chambers deduced by geochemical studies at 1–3 km depth (Marianelli et al., 1999) were possibly formed at the occurrence of the eruption and were after depleted at the end the eruptive activity.

Acknowledgements

This work is financed by INGV-DPC (Dipartimento di protezione Civile Italiana) project V3_4. Routine analysis has been carried out in LAV (Laboratorio di Analisi aVanzate of INGV-Naples) by Simona Petrosino and Paola Cusano, who are gratefully acknowledged. Gilberto Saccorotti, Vincenzo Nisii, Anna Tramelli, Lucia Zaccarelli helped with numerous discussions. Three anonimous reviewers and the editor are gratefully acknowledged for their useful comments and suggestions that greatly improved the paper.

References

Aki, K., 1980. Attenuation of shear-waves in the lithosphere for frequencies from 0.05 to 25 Hz. Phys. Earth Planet. Inter. 21, 50–60.

Berrino, G., Coppa, U., De Natale, G., Pingue, F., 1993. Recent geophysical investigation at Somma–Vesuvius volcanic complex. J. Volcanol. Geotherm. Res. 58, 239–262.

Bianco, F., Castellano, M., Del Pezzo, E., Ibanez, J.M., 1999. Attenuation of short period seismic waves at Mt. Vesuvius. Italy Geophys. J. Int. 138, 67–76.

Capuano, P., Gasparini P., Zollo A., Virieux J., Casale R., Yeroyanni M., 2003. The internal structure of Mt. Vesuvius. A seismic tomography investigation. Liguori Editore ISBN 88–207-3503–2.

Cassano, E., La Torre, P., 1987. Geophysics, in Somma-Vesuvius. Editore R. Santacroce, CNR quaderni 114, Roma, 175–196.

Del Pezzo, E., Bianco, F., Saccorotti, G., 2004. Seismic source dynamics at Vesuvius volcano, Italy. J. Volcanol. Geotherm. Res. 133, 23–39.

Del Pezzo, E., Bianco, F., Zaccarelli, L. Separation of Qi and Qs from passive data at Mt. Vesuvius: a reappraisal of seismic attenuation. Phys. Earth Planet. Inter., submitted for publication.

Gusev, A.A., Abubakirov, I.R., 1999. Vertical profile of effective turbidity reconstructed from broadening of incoherent body-wave pulses. Geophys. J. Int. 136, 309–323.

Lawson, C.L., Hanson, R.J., 1974. Solving least squeres problems. Prentice-Hall, inc., New Jersey.

Lees, J.M., Crosson, R.S., 1989. Tomographic inversion for three-dimensional velocity structure at Mount St. Helens using earthquake data. J. Geophys. Res. 94, 5716–5728.

Lomax, A., Zollo, A., Capuano, P., Virieux, J., 2001. Precise absolute earthquake location under Somma-Vesuvius volcano using a new three-dimensional velocity model. Geophys. J. Int. 146, 313–331.

Marianelli, P., Métrich, N., Sbrana, A., 1999. Shallow and deep reservoirs involved in magma supply of the 1944 eruption of Vesuvius. Bull. Volcanol. 61, 48–63.

Sato, H., Fehler, M.C., 1998. Seismic Wave Propagation and Scattering in the Heterogenous Earth. Springer.

Scandone, R., Giacomelli, L., Gasparini, P., 1993. Mt. Vesuvius: 2000 years of volcanological observations. J. Volcanol. Geotherm. Res. 58, 5–26.

Scarpa, R., Tronca, F., Bianco, F., Del Pezzo, E., 2002. High resolution velocity structure beneath Mount Vesuvius from seismic array. Geophys. Res. Lett. 29 (21), 2040.

Tichelaar, B.W., Ruff, L.R., 1989. 1989 How good are our best models? EOS 70, 593–606.

Zollo, A., D'Auria, L., De Matteis, R., Herrero, A., Virieux, J., Gasparini, P., 2002. Bayesian estimation of 2-D P-velocity models from active seismic arrival time data: imaging of the shallow structure of Mt. Vesuvius (Southern Italy). Geophys. J. Int. 151, 566–582.